Atmos. Chem. Phys. Discuss., https://doi.org/10.5194/acp-2019-34
Manuscript under review for journal Atmos. Chem. Phys.
Discussion started: 1 February 2019

Atmospheric Chemistry and Physics
Discussions

On the distinctiveness of oceanic raindrop regimes

David Ian Duncan[1], Patrick Eriksson[1], Simon Pfreundschuh[1], Christian Klepp[2], and Daniel C. Jones[3]

[1]Department of Earth, Space, and Environment, Chalmers University of Technology, SE 412 96 Gothenburg, Sweden
[2]CliSAP/CEN, Meteorological Institute, Universität Hamburg, 20146 Hamburg, Germany.
[3]British Antarctic Survey, CB3 0ET Cambridge, United Kingdom

Correspondence: David Ian Duncan (david.duncan@chalmers.se)

Abstract. Representation of the drop size distribution (DSD) of rainfall is a key element of characterizing precipitation in models and retrievals, with a functional form necessary to calculate the precipitation flux and the drops' interaction with radiation. With newly available oceanic disdrometer measurements, this study investigates the validity of commonly used DSDs, potentially useful a priori constraints for retrievals, and the forward model errors caused by DSD variability. These data are also compared to leading satellite-based estimates of oceanic DSDs. Forward model errors due to DSD variability are shown to be significant for both active and passive sensors. The modified gamma distribution is found to be generally adequate to describe rain DSDs, but may cause systematic errors for high latitude or stratocumulus rain retrievals; depending on the application, an exponential or generalized gamma function may be preferable for representing oceanic DSDs. An unsupervised classification algorithm finds a variety of DSD shapes that differ from commonly used DSDs, but does not find a singular set that best describes the global variability. Finally, DSD shapes are found to be not particularly distinctive of regional or large-scale environments, but rather occur at varying frequencies over the global oceans.

1 Introduction

A challenge shared by atmospheric models and remote sensing retrievals alike is the representation of precipitation microphysics. Raindrops can be modeled using a variety of functional forms, simple relations between drop size and number density that attempt to capture the bulk behavior in a way sufficient to represent the processes of interest. The radiative characteristics and precipitation flux through an atmospheric volume containing precipitation depend on the size and resulting terminal velocities of the rain drops, defined via that volume's drop size distribution (DSD). In this way, the DSD acts as a necessary conduit to represent precipitation processes, one common to climate models, radar retrievals, and data assimilation schemes.

Various functional forms have been employed to describe rain DSDs. Exponential DSDs (Marshall and Palmer, 1948) have been common in radar meteorology for decades, and different versions of the modified gamma distribution (MGD; Eq. 1) have gained popularity for remote sensing (Ulbrich, 1983). Simplifications of the MGD to three, two, or single parameter versions yield the gamma, exponential, and power law relations (Petty and Huang, 2011), respectively, all of which are used to represent DSDs in various applications. Between those who use the MGD to describe DSDs, disagreement exists on how many free parameters to use (Smith, 2003; Thurai and Bringi, 2018), whether it is best to normalize the distribution (as in Eq. 3) in some way (Testud et al., 2001), or if the separation of parameters in the MGD is either physically meaningful or outperformed by simpler methods (Williams et al., 2014; Tapiador et al., 2014).

The below equations will be referred to throughout the text as the generic MGD function (Eq. 1) and normalized gamma function (Eq. 3), with $N(D)$ the number of drops per volume per size as a function of the drop diameter, D (with D given in mm and $N(D)$ in $\mathrm{mm^{-1}\,m^{-3}}$). N_0 and N_w are intercept parameters and μ is the shape parameter, though N_w is a normalized intercept parameter. D_m is the mass-weighted mean diameter, the ratio of the fourth and third moments of the distribution (Eq. 2). Γ is the gamma function, ρ_w is the density of water, and RWC is the rain water content in $\mathrm{kg\,m^{-3}}$.

$$N(D) = N_0 D^{\mu} e^{-\lambda D^{\gamma}} \tag{1}$$

$$D_m = \frac{\int_0^\infty N(D) D^4 dD}{\int_0^\infty N(D) D^3 dD} \tag{2}$$

$$N(D) = N_w f(\mu) (\frac{D}{D_m})^{\mu} e^{-(4+\mu)\frac{D}{D_m}}, \quad f(\mu) = \frac{\Gamma(4)}{4^4} \frac{(4+\mu)^{4+\mu}}{\Gamma(4+\mu)}, \quad N_w = \frac{4^4}{\pi \rho_w} \frac{RWC}{D_m^4} \tag{3}$$

Scattering of radiation is highly dependent on particle size, and thus the DSD is a crucial component of remote sensing retrievals, whether it is assumed or retrieved. Depending on the application, the specific choice of DSD may or may not make much difference (e.g. Smith (2003); Illingworth and Blackman (2002)). For instance, erroneous assumptions about small drops may not impact the bulk radiative fluxes or precipitation characteristics of a volume, but a more accurate DSD representation may be necessary when considering additional frequencies or polarized measurements. The under-constrained nature of precipitation retrieval means that the DSD is either assumed completely or needs to be quite constrained to allow tractable solutions.

A lack of globally representative DSD data has hampered the retrieval of precipitation from satellites. Satellite retrievals rely heavily on a priori knowledge to constrain the solution space, and regional differences in meteorology and microphysics can manifest as regional biases in satellite retrievals (Berg et al., 2006). Whereas ground radar networks and arrays of disdrometers over land have helped to characterize the variability of raindrops from continental precipitation (e.g. Bringi et al. (2003); Williams and Gage (2009); Thurai and Bringi (2018)), observations of DSDs over ocean have mostly been limited to field campaigns and coastal radar retrievals. Because of the different aerosol loading, convective strength, and underlying humidity of airmasses over land, oceanic drop populations can be quite distinct from those over land, with the different microphysics influencing satellite retrievals (Petković et al., 2018).

It is expedient to condense the variability of DSDs into a few distinct classes, either to narrow the possible solution space of remote sensing retrievals or for interpretation of results. Separation of stratiform and convective precipitation has long been common, as stratiform precipitation tends to have a more peaked distribution of fewer, smaller drops versus the more exponential distribution of precipitation from convective clouds (Thurai et al., 2010; Thompson et al., 2015). However, partitioning

Atmos. Chem. Phys. Discuss., https://doi.org/10.5194/acp-2019-34
Manuscript under review for journal Atmos. Chem. Phys.
Discussion started: 1 February 2019

stratiform and convective rainfall is done in various ways and may differ depending on location. A little further, Dolan et al. (2018) argue for six dominant modes of DSDs globally, separated via principal component analysis but linked to meteorology and attendant microphysical regimes. As many studies of drop distributions are from land-based disdrometers and radars, DSD variability has been studied less over open ocean where a majority of global precipitation occurs, though advances are being made in this area (Thompson et al., 2018).

In remote sensing applications, one can attempt to solve for all, some, or none of the parameters that define a functional form such as Eq. 1, depending on the information content available. A normalized distribution such as Eq. 3 is used in many precipitation retrievals to separate the water content from the spectrum's shape. In that formulation with RWC separate, this leaves two free parameters to define the distribution since RWC is directly related to N_w through D_m. While passive-only retrievals may need to assume one of these parameters because of the limited signal available (Duncan et al., 2018), radar or combined radar/radiometer retrievals may solve for these parameters in a constrained way (Munchak et al., 2012; Grecu et al., 2016). Precipitation retrievals thus handle the complexity of the DSD differently depending on their sensitivity, but necessarily using a predefined functional form to limit the inverse problem's degrees of freedom.

To investigate the distinctiveness of raindrop shape regimes over the global oceans, and how these regimes may impact retrievals both in terms of prior constraints and radiative transfer modeling, the study proceeds as follows. Data and methods are described in the next section, introducing the disdrometer and satellite data examined, as well as the machine learning technique used to classify drop regimes. Section 3 presents a holistic view of global disdrometer measurements with respect to the normalized gamma distribution, including a comparison to the leading satellite-based, near-global DSD data set. Section 4 critically examines the disdrometer data versus a commonly used functional form and investigates how distinct raindrop regimes truly are. In Section 5 the radiative aspects of DSD variability are addressed in the context of satellite retrievals with radiative transfer modeling. The paper closes with some conclusions.

2 Data and Methods

2.1 OceanRAIN

The Ocean Rainfall And Ice-phase precipitation measurement Network (OceanRAIN) coordinates disdrometer measurements and acquired ancillary data aboard research ships across the global oceans (Klepp et al., 2018). The data set begins in 2010 and collection is ongoing, with observations spanning 8 vessels and over 6 million minutes covering all ocean latitudes. OceanRAIN data contain raw counts integrated for each minute of rain, snow, or mixed-phase precipitation, with derived rainfall DSD parameters fitting Eq. 3, and various ancillary fields. The large and growing size of the data set make statistical analysis possible due to its consistent application across various ships. The raw disdrometer data are integrated per minute and separated into logarithmically-spaced size bins, permitting analysis of DSDs without the assumption of a functional form. Specifically, the OceanRAIN-M data are used primarily in the study (Klepp et al., 2017), in which raw drop counts from the disdrometer are converted to number concentrations per size (i.e. drops per volume per size), the form in which DSDs are commonly given. DSD assumptions commonly made in the literature can thus be assessed against the unmolested observations.

Underpinning OceanRAIN is the ODM470 optical disdrometer, a sensor with sensitivity to hydrometeors of diameter 0.3 to $22\,\mathrm{mm}$ (Klepp, 2015). The disdrometer is deployed on the superstructure of ships in a package including a cup anemometer and a precipitation detector to activate the disdrometer. A wind vane turns the disdrometer to keep the optical path normal to the wind direction to minimize impacts of turbulence. Only data points marked as rain definite and with a probability of precipitation of 100% were used in the following analysis.

Simulated reflectivites from the ODM470 disdrometer have demonstrated high correlation and a near-zero bias when compared against co-located, vertically-oriented radar observations (see Fig. 6, Klepp et al. (2018)). In comparisons with co-located rain gauges, the optical disdrometer performs better in high wind speeds, as undercatch is a significant problem for traditional rain gauges that can result in underestimation of rainfall accumulation by 50% (Grossklaus et al., 1998; Klepp et al., 2018), though accumulations match within 2% for low wind speeds (Klepp, 2015). The ODM470 has been used in a variety of conditions and shown no difference in accuracy between oceanic and continental cases (Bumke and Seltmann, 2011).

The robustness of disdrometer-derived DSD parameters (following Eq. 3) will depend somewhat on the parameter discussed and the type of rain. For instance, derived D_m should be very robust for all but the very weakest rain rates as it is simply defined (Eq. 2) and requires no fitting. The accuracy of derived N_w may be suspect for cases with high rain rates and a low D_m value, as drops below the sensitivity threshold of $0.39\,\mathrm{mm}$ may constitute a non-negligible fraction of total drops, though this depends on the type of rainfall and is an issue faced by all disdrometers (Thurai et al., 2017). The derived shape parameter, μ, is the least robust of the three as it depends on a curve fitting which may not be optimal for very light rain rates or spectra that do not conform to the expected general shape.

2.2 GPM Combined

The Global Precipitation Measurement (GPM; Hou et al. (2014)) Core Observatory holds two sensors designed to measure precipitation: the GPM Microwave Imager (GMI) and the Dual-frequency Precipitation Radar (DPR). GMI is a passive microwave radiometer measuring from 10 to $190\,\mathrm{GHz}$ and the DPR is a phased array radar measuring at K_U and K_A bands (13.6 and $35.5\,\mathrm{GHz}$, respectively). The dual frequencies of DPR set it apart from other satellite-borne sensors as far as the capacity to solve for the DSD. The GPM core satellite's combination of passive and active sensors provides sensitivity to a large range of precipitating hydrometeors, with information on their emission and scattering characteristics.

The GPM combined algorithm (Grecu et al., 2016) is a retrieval that uses data from both radar and radiometer to solve for profiles of hydrometeors that optimally fit the observations. As the GPM core observatory represents the best observational platform yet flown for measuring near-global precipitation, the combined retrieval from DPR and GMI is included in this study as the state of the art for calculating global DSD statistics. Via the same DSD formulation given in Eq. 3, the combined retrieval first uses the K_U band reflectivities to solve for the D_m profile. It then retrieves N_w at a reduced vertical resolution to match the K_A band and deconvolved GMI brightness temperatures (T_Bs) using optimal estimation. The shape parameter is fixed at $\mu = 2$ for all cases. For further details about this retrieval, see Grecu et al. (2016).

In this study, gridded level 3 GPM Combined data are used (Olson, 2017). This data set provides statistics of pixel-level derived DSD parameters from Eq. 3 at 5° horizontal resolution. The values used in this study are from the lowest altitude bin and include oceanic pixels only so as to best match the ground-based data from OceanRAIN-M. Because GPM Combined receives most of its information content from DPR, the DSD parameters derived are representative of individual segments of the atmospheric column and not a column average, a key difference from passive-only retrievals. This is significant, as comparison with ground-based observations should be as close in altitude as possible, as DSDs will vary with altitude as evaporation, coalescence, collisions, or other processes modify the spectra (Williams, 2016). The $250\,\mathrm{m}$ vertical resolution of DPR means that multiple observations exist below $1\,\mathrm{km}$ altitude, though some of these will be affected by ground clutter and so the lowest bin without clutter is chosen here. Note that the GPM Combined retrievals were performed at the native DPR pixel size, which has a $5\,\mathrm{km}$ horizontal resolution.

2.3 Gaussian Mixture Modeling

Gaussian Mixture Modeling (GMM) is an unsupervised, probabilistic classification technique that attempts to represent a data set using a linear combination of multidimensional Gaussians in a chosen parameter space. The dimensions (or “features”) of the parameter space and the maximum number of classes, N_{GMM}, are set by the user. GMM assigns each data point to the class, represented by a multidimensional Gaussian function, with the highest posterior probability for that data point. For further technical details on GMM and its use in other Earth science applications, see Maze et al. (2017) and Jones et al. (2019). The Python package *scikit-learn* supplied the GMM code (Pedregosa et al., 2011).

GMM easily generalizes to a wide variety of data distributions and can thus identify structures in the data that might be missed by more traditional curve fitting methods. This frees the analysis from explicit assumption of a DSD shape such as Eq. 3. In the approach used here, the “dimensions” given to the GMM module are the size bins used by the OceanRAIN disdrometers and thus the input data are an array of approximately 90000 raining minutes with 60 size bins. These data are unchanged other than being normalized so that DSD “shape” variability in the data set is not weighted by the total number of drops observed, and cut off at 60 size bins as very few drops over $5\,\mathrm{mm}$ are ever measured. Because the shapes are independent of the total number of drops, this is analogous to the normalized DSD approach typified by Eq. 3. GMM thus finds common shapes of the observed DSDs and determines the posterior probability of each data point (DSD for each raining minute) falling into each of the various classes. Each observed DSD is assigned to the GMM class for which it has the highest posterior probability. The resultant classes provide insight into dominant structures of the input data, with this approach exemplified in Section 4.2.

The number of GMM classes is set a priori, with the degree of complexity described by the GMM decomposition dependent on the number of states set by the user. Determining an optimal value for N_{GMM} is thus important but somewhat subjective because the desired level of complexity retained after the decomposition will vary for different applications. One method for estimating a suitable range for the number of classes is to use the Bayesian Information Criterion (BIC; Eq. 4). This metric contrasts the log likelihood (L) against a cost for the number of classes (K) to provide an objective measure of how many classes should optimally describe the data, where $N_f(K) = K - 1 + KD + KD(D-1)/2$, with D the dimension of the data space and n the number of data points used in model training. The first term in Eq. 4 becomes more negative with increased likelihood, while the second term acts to penalize overfitting. The minimum BIC thus signifies the optimal K value, maximizing the variability explained with the fewest possible classes. A plateau of BIC values versus K would signify no distinctly optimal K to describe the data's variability, but rather a range of solution spaces in which the addition of further states provides marginal additional complexity.

$$BIC(K) = -2L(K) + N_f(K)log(n) \tag{4}$$

3 Global DSD observations

3.1 Disdrometer data

Viewing the OceanRAIN data all together can provide a sense of the variability in DSD populations over the world's oceans. From the perspective of global retrievals, constraints on the DSD that depend on the location or environmental regime, rather than, say, partitioning stratiform and convective precipitation a priori, are useful for independent satellite-based products that do not ingest detailed model data, such as the operational retrievals for the GPM constellation radiometers (Kummerow et al., 2015). To this end, the derived parameters of Eq. 3 are given for all raining disdrometer observations in Fig. 1. As this is the DSD form most used in rainfall retrievals currently, it is presented here.

As seen in Fig. 1, the normalized gamma DSD parameters exhibit a wide range of variability that is not strongly tied to location. The strongest trend visible is that warmer ocean surfaces witness greater densities of drops, with the mean $log_{10}(N_w)$ increasing from about 3.5 to 4.0. This is roughly in line with the a priori N_w used for rain by Mason et al. (2017) of $3.9e3$, or 3.59 in log space. It is noted that the distributions of D_m and μ are not particularly Gaussian, with the means and medians separate, and N_w only moderately Gaussian in log space.

It is stressed that OceanRAIN observations are not evenly distributed around the global oceans and thus the values seen are dependent on the sampling (i.e. where the ships sailed), so these values are not fully representative of each ocean latitude band. As surface-based observations they do not provide information as to any vertical DSD variability, a topic that requires radar observations (Williams, 2016). However, it is possible to pick out some meteorological regimes of interest from the derived DSD parameters in OceanRAIN. For instance, the ships' heavy sampling of Southern Hemisphere stratocumulus regions shows up in these plots as a regime characterized by a higher number of small drops and a more peaked distribution (seen in the 20°S to 40°S band in Fig. 1). From the perspective of satellite rainfall retrievals, such location- or cloud regime-dependent a priori constraints are much preferable to a global prior and useable within existing algorithms.

3.2 Comparison to GPM

As mentioned in Section 2.2, GPM is the best satellite-borne platform currently available for measuring DSD variability, and thus the best near-global observational DSD data set for comparison. To assess the similarity between GPM estimates and the in situ disdrometer measurements of OceanRAIN, here the retrieved results for N_w and D_m are compared, as the GPM retrieval assumes a constant μ value. To perform this comparison, histograms of level 3 GPM Combined data at 5° resolution

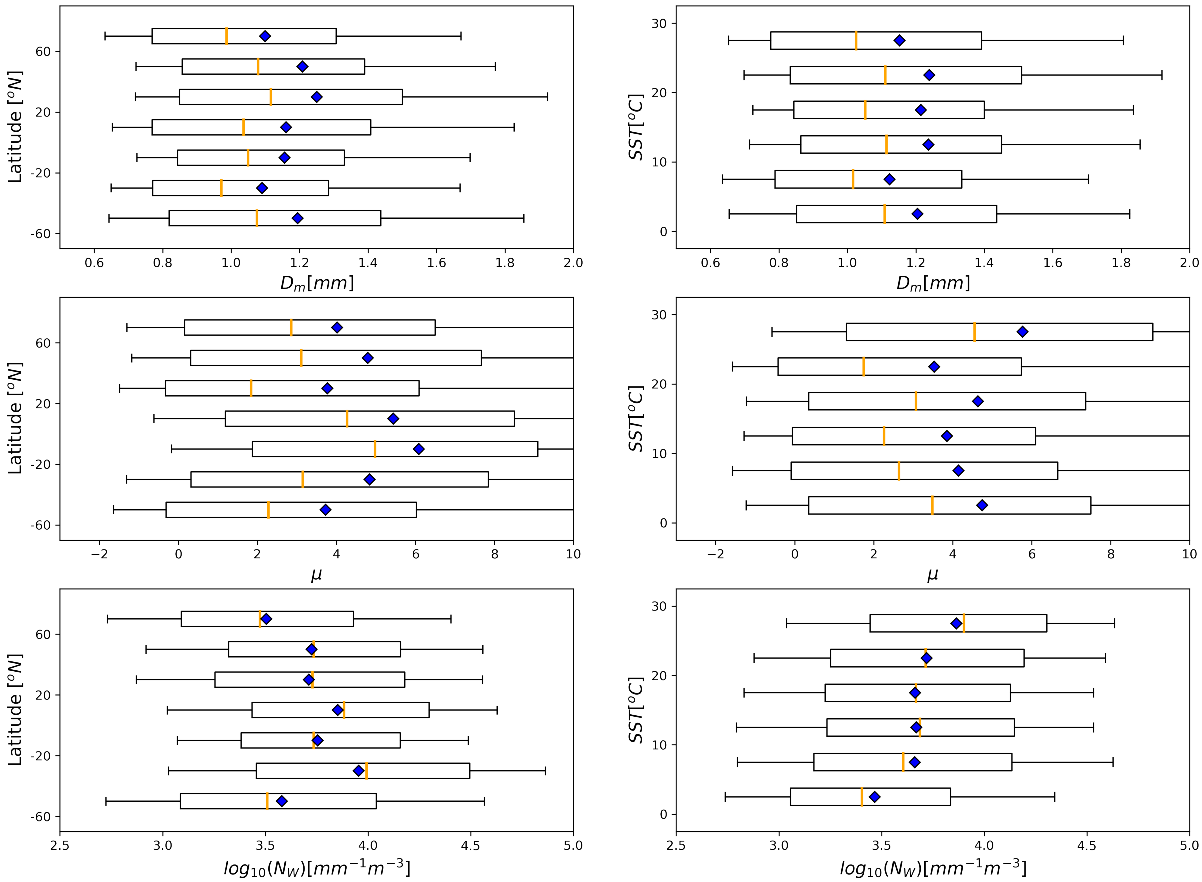

Figure 1. Distribution of DSD parameters following Eq. 3. The boxes define the standard deviations ($\pm 1\sigma$), the whiskers define the 10% and 90% bounds, orange lines denote the median, and blue diamonds the mean. Observations are divided according to latitude (left) and sea surface temperature (right).

were used, spanning 12 months from 2017. Due to the uneven sampling of the ship-borne disdrometers, the only GPM data included in the analysis are from months with valid OceanRAIN data points in each box and defined as ocean pixels by DPR. No attempt was made to match observations exactly in space and time due to the difficulty of point-to-area comparisons with ship-borne data and GPM (Burdanowitz et al., 2018; Loew et al., 2017).

The left panel of Fig. 2 shows histograms of derived D_m from the disdrometers compared with GPM Combined, separated by latitude. Given the limited sensitivity of DPR to small drops, it is unsurprising to note that OceanRAIN observes a wider distribution of D_m that is most noticeably distinct from GPM results for small drops. Another key feature of these histograms is that while the maxima in D_m distributions are relatively similar for the two data sets, OceanRAIN observes a much less peaked distribution with a longer tail for larger drops in most latitudes. In the 40° to 60° latitude bin for both hemispheres GPM has a more bimodal distribution. For all latitudes GPM exhibits a strong peak near $D_m = 1\,\mathrm{mm}$.

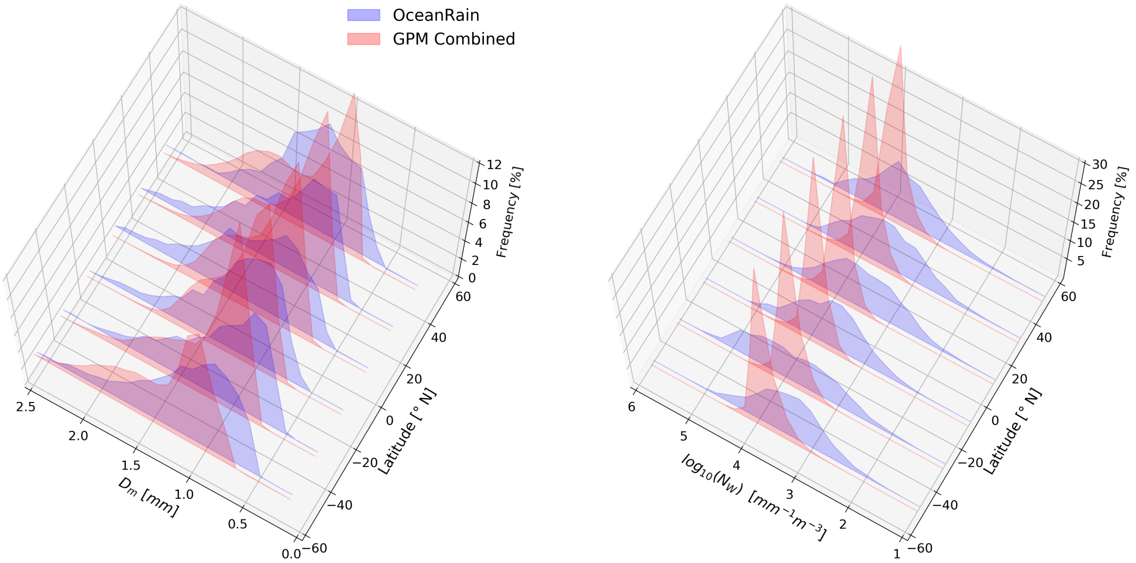

Figure 2. Histograms of D_m (left) and N_w (right) for GPM Combined and OceanRAIN, separated by latitude. GPM data are from the 3B CMB monthly gridded product.

The right panel of Fig. 2 follows the same format but for derived N_w. The most striking aspect of these histograms is the strongly peaked distribution retrieved by GPM in all locations. In contrast, the disdrometers observe many cases with N_w values an order of magnitude greater or smaller than those of the GPM distributions. This would appear to have two leading, plausible explanations. First, OceanRAIN is expected to observe more variability in the number of drops because it is a point measurement integrated over one minute and precipitation characteristics can vary widely over multiple kilometers, whereas DPR has a $5\,\mathrm{km}$ footprint. Second, DSD retrieval from GPM is very much an under-constrained problem despite the unique capabilities of DPR. While the altitude mismatch between ground-based disdrometers and the GPM data at a few hundred meters altitude may cause some systematic differences, say due to some evaporation unseen by GPM, this does not explain the limited range of N_w values retrieved by GPM. The strongly peaked N_w distributions seem indicative of the significant influence of the a priori state on retrieval of N_w, in addition to the limited sensitivity to small number concentrations dictated by the instrument sensitivity of DPR.

4 Applicability of the modified gamma distribution

4.1 Overall behavior

Without applying any sorting methods or functional forms to the OceanRAIN data, it is worth viewing the data as a whole to see how closely the bulk behavior resembles the distributions commonly used in the literature. Figure 3 shows a two-dimensional probability density function (PDF) of drop diameter normalized by D_m versus number concentration normalized by N_w. This is a view of bulk behavior often used to justify usage of the MGD for precipitation (Bringi et al., 2003; Leinonen et al., 2012), as it permits visualization of in situ data points with the MGD for various μ values including the exponential DSD. Figure 3 indicates that much of the spectral power within OceanRAIN lies near the exponential (μ=0) line or near the lines with small shape parameters. This is consistent with the enduring popularity of exponential DSDs and the $\mu = 2$ assumption of GPM Combined.

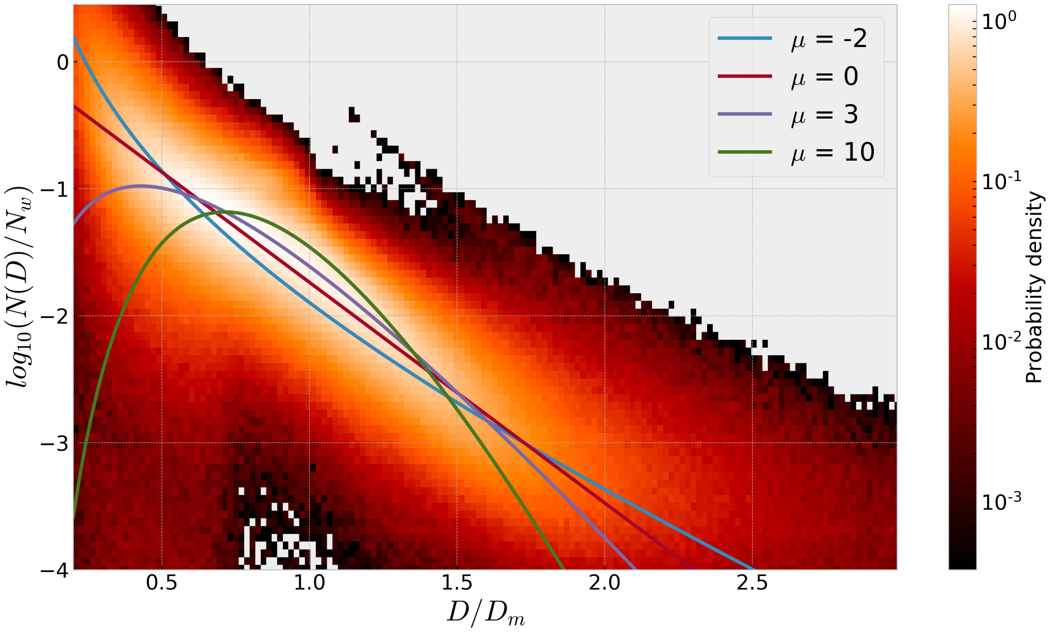

Figure 3. Probability density function of all raining OceanRAIN data points, visualized using the scaled DSD, $N(D)/N_W$, against the diameter-normalized by D_m. Various curves with prescribed μ values are plotted for comparison. Areas in gray indicate no data.

To examine the applicability of the normalized gamma distribution to observed ocean DSDs, we can compare the observed PDF (Fig. 3) with the PDF generated after performing the 3-parameter MGD fit. This is shown in Fig. 4(a), with sample MGD curves given for extreme values of the shape parameter. The MGD-derived PDF overestimates the frequency of points near the exponential line and understandably displays less spread; blue areas indicate over-representation from the MGD fit, red areas indicate under-representation from the MGD fit. As with comparison between the PDF and MGD curves in Fig. 3, this shows an underestimation of small drops at high number concentrations through virtue of being constrained by the MGD fit. To see if there is some regional dependence within the overall OceanRAIN PDF, Fig. 4(b) divides the data into observations from high latitude (latitudes greater than 50°) and tropical (latitudes less than 20°) locations. It appears that whereas the MGD with a shape parameter ranging from $\mu = 0$ to $\mu = 3$ suffices for many tropical cases, high latitude observations are not always well represented by this formalism. For high latitude oceanic rainfall, Fig. 4(b) demonstrates that small drops are underestimated and medium drops overestimated if using the MGD with 3 moments or fewer.

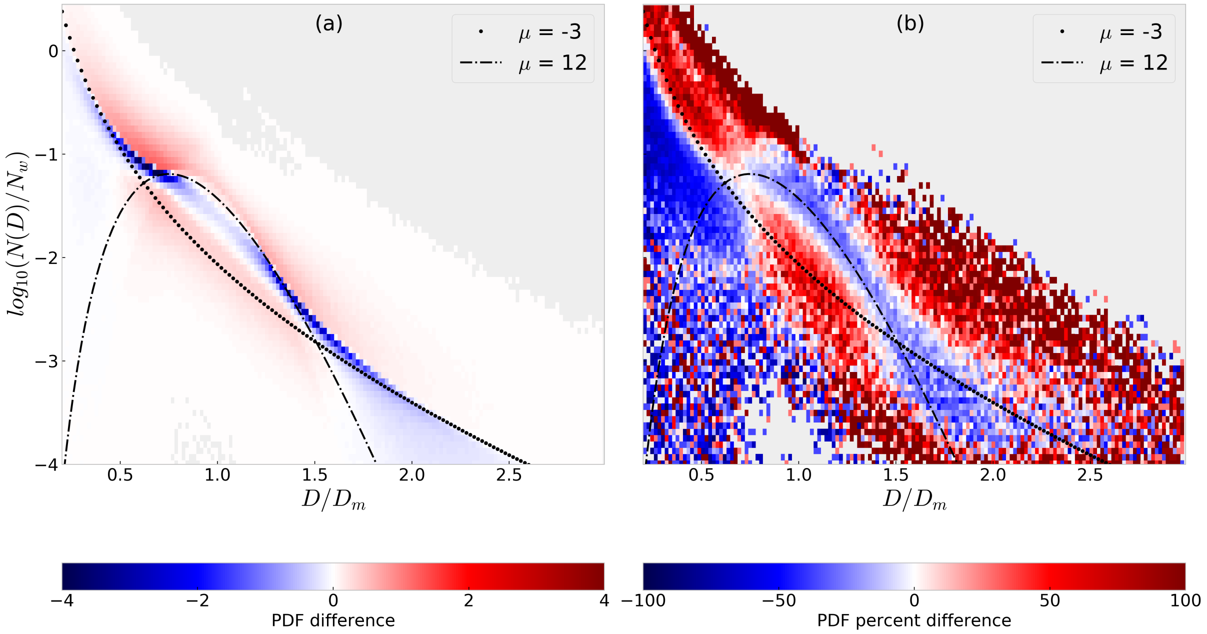

Figure 4. As in Fig. 3, but differences of PDFs. The left panel (a) shows the MGD-fitted PDF subtracted from the full OceanRAIN PDF shown in Fig. 3. The right panel (b) shows the difference of OceanRAIN PDFs from high latitude and tropical oceanic locations, viz. $PDF_{>50^\circ} - PDF_{20^\circ N - 20^\circ S}$, given as a percent difference. Areas in gray indicate no data in one or both PDFs. The low and high μ curves given approximately bound the PDF space for the MGD-fitted data.

One concern raised by the results of Fig. 4 is whether the use of the MGD, and its limited representation of the full PDF of drop sizes, can cause biases in modeled or retrieved rain rates. To examine this is quite straightforward, in that a size-dependent terminal velocity (Atlas and Ulbrich, 1977) can be assigned for drops of each size bin, with the rain rate calculated as the integral product of the velocity distribution and the third moment of $N(D)$. This can then be compared between DSD representations. Using all raining OceanRAIN observations, use of the MGD fit was found to result in a small overestimation of rain rates, by $0.06\,\mathrm{mm\,h^{-1}}$ or 1.9%. Using the same definitions as above, this underestimation was slightly less pronounced at high latitudes than for tropical locations, 1.5% versus 2.1%. This is due to underestimation of small drops by the MGD fit, as small drops have lower terminal velocities than larger drops, and with RWC being equal this can have a minor impact on resultant fluxes of precipitation.

Much of the spread that exists in the full OceanRAIN PDF is due to the use of raw observational data that contain discontinuities between size bins and some degree of instrument error. It is clear, however, that much of the spectral power in Fig. 3 is not captured by any one MGD curve. While the exponential line and $\mu = 3$ curves do a reasonable job at matching the PDF for larger drop sizes, the $\mu = -2$ curve performs much better for smaller diameters. This suggests that a 4-parameter "generalized gamma" fit might be optimal for ocean DSDs, a finding echoed in another recent study of disdrometer data (Thurai and Bringi, 2018). Use of the 3-parameter MGD can lead to some systematic biases in drop size representation as seen in Fig. 4(a). These biases can be regionally dependent, as shown by the higher number concentrations of small drops seen in high latitudes relative to the tropics, as seen in Fig. 4(b).

4.2 GMM states

As shown in Fig. 3, the MGD with a low μ value does a reasonable job at capturing the main power of the observed PDF. However, a great deal of spread exists that is not captured by any one curve. With this in mind, GMM was employed to investigate if a finite number of DSD shapes without a predefined functional form could better capture this variability. To provide a visualization of how the GMM states attempt to fit the observed DSD from the disdrometer, and how these states compare with various MGD forms, Fig. 5 contains randomly sampled data points from OceanRAIN. The GMM curves shown are from iterations with N_{GMM} of 6 and 14, two of the panels given in the subsequent figure; these are the states with the highest posterior probability from GMM, indicating the best match to the observed distribution. No fitting was performed (other than scaling by the correct RWC), just the most similar GMM curve was chosen. Also provided for reference are MGD curves with 1-, 2-, and 3-moment fits. The MGD 1- and 2-moment fits represent RWC-only and RWC and D_m fits, respectively, with a nominal shape parameter assumed. All the curves in Fig. 5 have the correct RWC as measured by the disdrometer.

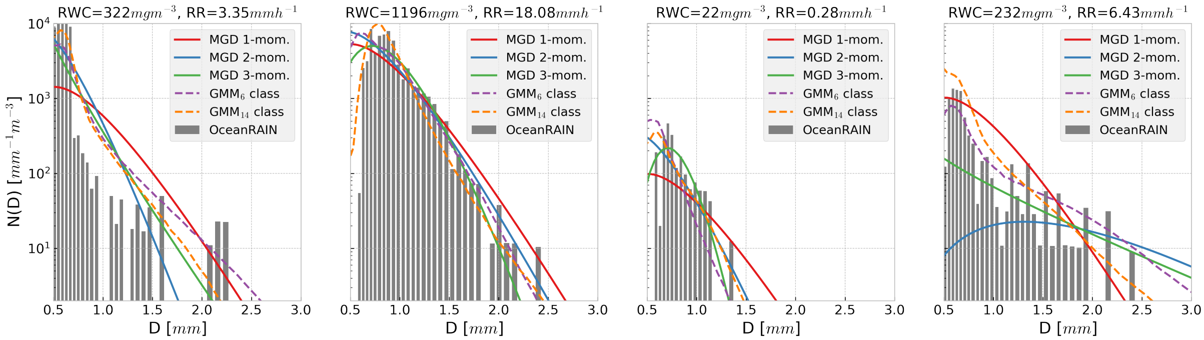

Figure 5. Each panel gives an OceanRAIN observed DSD, with concentrations shown in the solid bars. Various fitted curves with identical RWCs are also given, including GMM-derived DSDs for N_{GMM} of 6 and 14, and 3 MGD curves. For the 1-moment MGD and GMM curves only RWC is provided, and for the 1- and 2-moment MGD curves $\mu = 3$. The 2-moment MGD has the correct D_m while the 3-moment MGD also has the fitted μ.

In contrast to the example plots of Fig. 5, Fig. 6 shows the mean GMM curves that arise from running GMM with a few different N_{GMM} values. Again, this is from running GMM on the raw disdrometer data, with only the number of classes set a priori. For comparison, reference lines of MGD with sample μ values are also given. Note that for each panel in Fig. 6, a majority of the GMM-derived DSDs feature more small drops than given by even the exponential ($\mu = 0$) line. In the simplest case with only two classes possible (first panel of Fig. 6), the DSD shape that best captures the majority of the OceanRAIN data set's variability (at least in terms of frequency of occurrence) is a shape that is more sloped than the exponential DSD, with many small drops and very few large drops. This particular shape is common to all the GMM realizations, with even more steeply sloped curves found as GMM states are added.

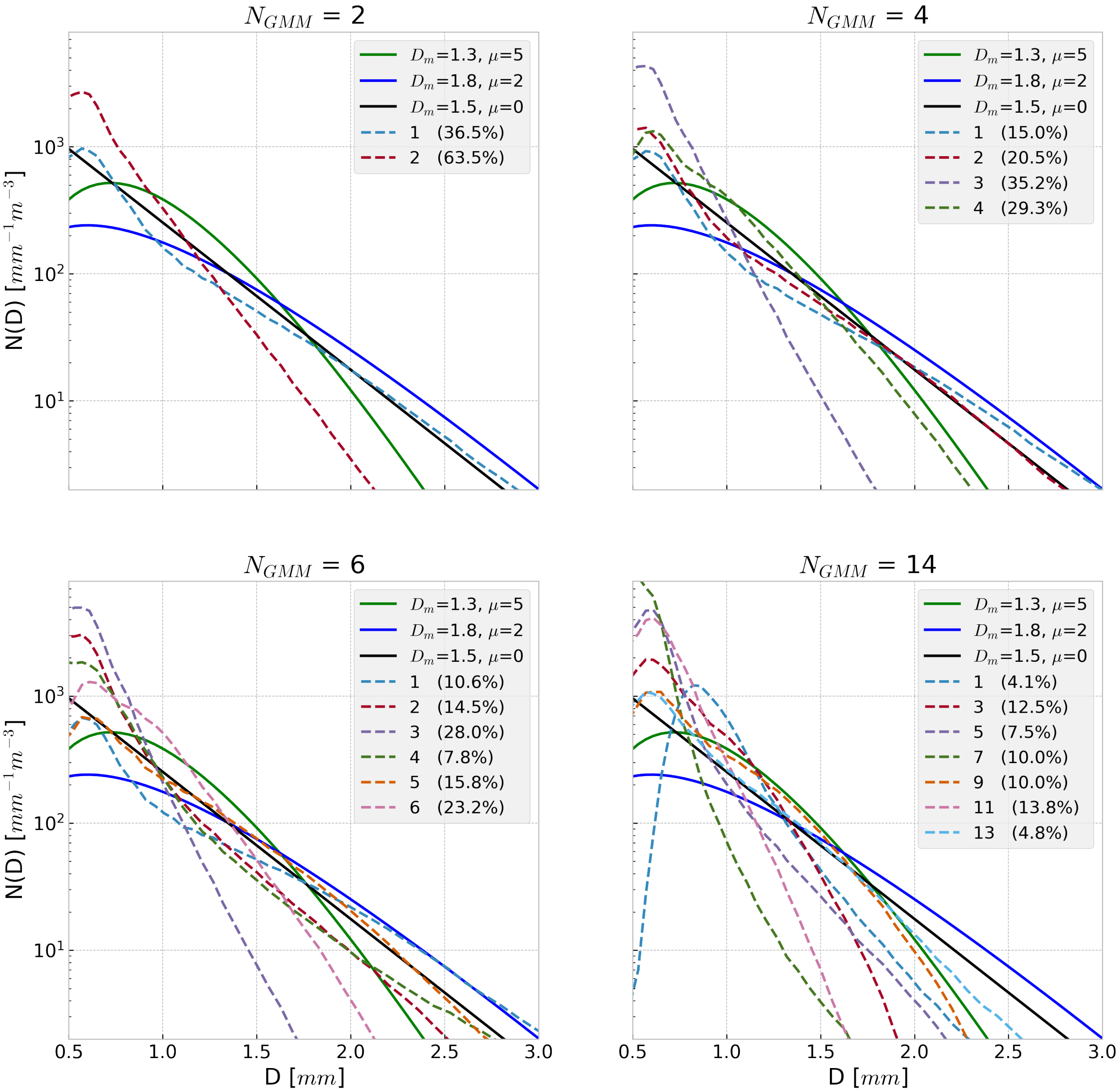

Figure 6. Panels show resultant DSDs for different GMM realizations ranging from N_{GMM} of 2 to 14. The last panel shows only odd numbered GMM states to reduce clutter. Each panel has an identical set of MGD curves with different μ and D_m values. All curves shown have the same water content. The frequency of occurrence for each GMM shape is given in the legend as a percentage.

It is noteworthy that most of the GMM states shown in Fig. 6 are not similar to the given MGD curves across the full range
5 of drop diameters. So while some of the GMM states are quite like a particular MGD curve over part of the domain, it is rare to

have DSD shapes from individual observations that resemble a 3-moment MGD across the whole size domain. In many cases the GMM method prefers states with more steeply sloped DSDs and more small drops than the sample MGD curves given. In fact, it takes higher values of N_{GMM} (such as in Fig. 6 with N_{GMM}=14) before strongly peaked DSD shapes reminiscent of MGD with a large μ value emerge. In other words, DSDs with few small drops, a strong peak of drops around D_m, and for which an exponential is a very poor approximation, are not very common. This can also be seen in Fig. 3, as scant spectral power is seen near the bottom left of that plot.

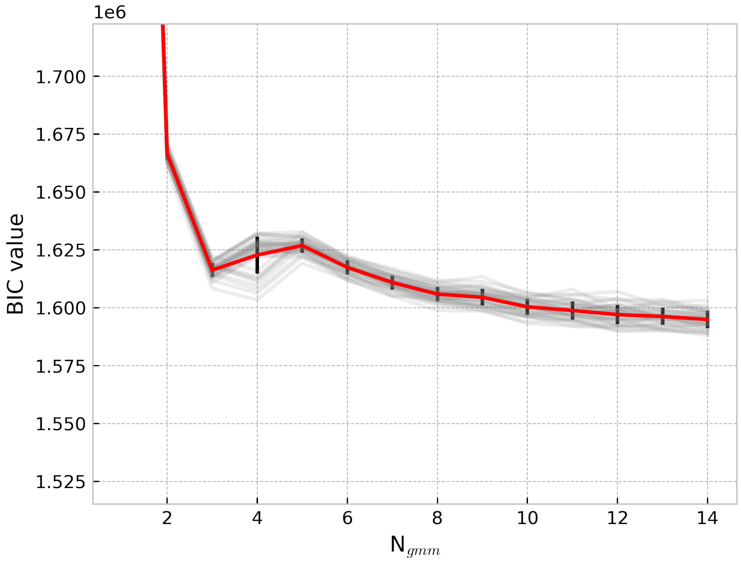

Figure 7. Bayesian Information Criterion (BIC) for different N_{GMM} choices applied to OceanRAIN. The mean BIC is shown in red with the standard deviation in black. Gray lines indicate GMM tests with limited samples, each a randomly chosen subset making up a third of the total data set.

The GMM framework as applied to the DSD problem seems to offer the promise of finding a finite number of distinct shapes with which global DSD variability can be described, a la Dolan et al. (2018), with the benefit of not constraining the type of shapes found. To investigate this, GMM was used in many iterations for randomly sampled subsets of the data to assess if an optimal number of states exist that describe the global shape variability. In this experiment N_{GMM} was varied from 2 to 12. The Bayesian Information Criterion (Eq. 4) gauges whether adding further states better describes the data or not, shown in Fig. 7. BIC plateaus and continues a slight decrease for GMM states beyond about $N_{GMM} = 8$, indicating that there is no singular set of GMM-derived DSD shapes that outperforms the others. Instead, oceanic DSD shape variability proves to be a true continuum that is not easily decomposed into a linear combination of a finite set of curves.

A corollary of the finding that a singular, optimal set of GMM-derived curves does not exist is that the observed DSD shapes do not display particularly predictable regional patterns. The shapes observed are not especially distinct when decoupled from RWC whether considering the DSDs regionally or say across SST regimes. The GMM-derived shapes are not particularly tied to one region or another, a finding that echoes Fig. 1. This is in contrast to some studies' success in pulling regional attributes out of large data sets via GMM without including location information, as done here (Jones et al., 2019). The only area of OceanRAIN sampling that is particularly distinct in the distribution of GMM states is from observations in stratocumulus regions, where the GMM states characterized by steeply sloped DSD curves with a large number of small drops are dominant. Otherwise, the GMM states are not strongly tied to particular sampling regions. This tendency changes if DSD is not decoupled from RWC, as RWC regimes are more tied to regional meteorology. But with respect to the retrieval problem, where it is convenient to separate the DSD shape from RWC as in Eq. 3, the GMM approach does not provide a magic bullet.

5 Radiative transfer impacts

An overlooked aspect of assuming a DSD a priori, or even just assuming the general shape of the DSD a priori, is that this will introduce forward model errors in retrievals and data assimilation. These errors can be strongly correlated across nearby frequencies and can thus cause systematic biases in variational systems if not taken into account. An example of including this type of forward model error into a variational rainfall retrieval for GPM was presented by Duncan et al. (2018). Instead, the focus in this section is investigating the extent of forward model response inherent to variations in natural drop populations, without fitting a functional form to the observed drop counts. Because water content or rain rate is usually the sought parameter from remote sensing retrievals, the results are separated along those lines.

The Atmospheric Radiative Transfer Simulator (ARTS) version 2.3 (Eriksson et al., 2011; Buehler et al., 2018) was used to perform forward model simulations. The ARTS model can handle custom particle size distributions and habits as well as prescribed DSDs such as the MGD. Thus with the full raw data from OceanRAIN it is possible to simulate the interaction of radiation with drop populations without making any simplifications involving the drops' functional form. To approximate the impact on a sensor such as GMI on GPM, simulations were run using the GMI geometry and three GMI frequencies: 18.7, 36.64, and 89.0 GHz. Because the surface-based disdrometer data inherently lack vertical information, hydrometeor and humidity profiles need to be assumed. To avoid complications from inclusion of any ice scattering species, the setup is for warm rain: a $1\,\mathrm{km}$ rain layer defined by the RWC and DSD observed, with a $1\,\mathrm{km}$ liquid cloud layer of $200\,\mathrm{g\,m^{-2}}$ above characteristic of a raining warm cloud (Lebsock et al., 2008). The surface properties and humidity profile are typical of a tropical scene, with the surface emissivity calculated using TESSEM2 (Prigent et al., 2017). DSD properties are constant within the rain layer and the cloud layer is also homogeneous. Simulation code is available (Duncan, 2019).

Figure 8(a) shows the results of the GMI simulations using native disdrometer data, with rain water path (RWP) simply RWC integrated over the $1\,\mathrm{km}$ rain layer. The change in radiance, ΔT_B, is defined relative to the non-raining case of $RWP = 0$ and for unpolarized radiation. With no mixed phase or ice phase hydrometeors in the atmospheric column, the three GMI channels chosen all exhibit a net increase in T_B. The $89\,\mathrm{GHz}$ shows little impact from either DSD variability or an increase in RWP, as its signal is mainly from cloud water emission, as the scattering from rain largely cancels out its emission signal. In contrast, the lower frequency channels show large increases in T_B with RWP as emission dominates and the cloud is more transparent, with the wide range of scattering response showing the strong dependence on drop size. The $18\,\mathrm{GHz}$ T_B especially shows large

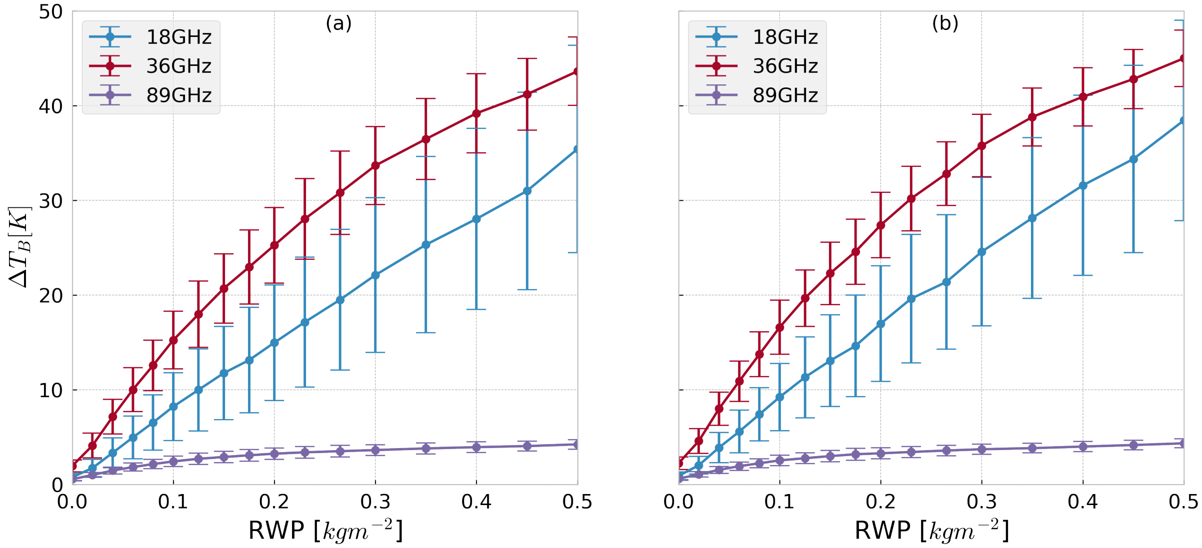

Figure 8. Simulated brightness temperatures through a modeled atmosphere for warm rain, with a liquid cloud layer of $200\,\mathrm{g\,m^{-2}}$ from 1 to $2\,\mathrm{km}$ altitude and rain in the lowest kilometer. The water content in the rain layer and the DSD are directly from disdrometer observations and constant in the rain layer. Given are the means and standard deviations ($\pm 1\sigma$) of ΔT_B per rain water path (RWP) bin, where the difference in T_B is defined relative to $RWP = 0$. The left panel (a) uses all OceanRAIN observations, the right panel (b) shows results when averaging over consecutive 6 minute observation windows to approximate a satellite footprint.

variability for a given RWP, with the standard deviation of the T_B response usually about half of the net response. This is a significant error source for warm rain estimation, as the difference between a RWP of 0.2 and $0.3\,\mathrm{kg\,m^{-2}}$ would be difficult to distinguish using these frequencies alone due to the overlapping forward model error bounds.

To address the point-to-area issue of comparing OceanRAIN observations integrated every minute with those of a spaceborne passive microwave or radar footprint, which is $5\,\mathrm{km}$ in the best case, Fig. 8(b) shows a sample result if the disdrometer data are averaged in time. Averaging in time is performed because it approximates a spatial average, absent other observing points. Specifically, a nominal 6 minute window was used to average consecutive raining disdrometer measurements. Non-raining points were not included or added if the OceanRAIN points were discontinuous in time. Fig. 8(b) shows that the results are quite similar to the native disdrometer data used in panel (a), and thus the maximum forward model errors observed by a sensor such as GMI should not be markedly different.

Without needing to assume a model atmosphere, the variability of radar reflectivities can be simulated with the measured volume of drops alone and the T-matrix method (Klepp et al., 2018). Figure 9 gives the simulated radar reflectivity response over a range of rain rates using the OceanRAIN observations. As with the passive sensor simulations, this demonstrates that DSD variability can cause significant differences in the radiative properties of a volume of drops even for equivalent rain rates or water contents. As with Fig. 8, the range of scattering response is larger for the lower frequency channels, with K_U showing greater variability in modeled reflectivity, as the specifics of the DSD determine whether the drops' scattering is wholly in the

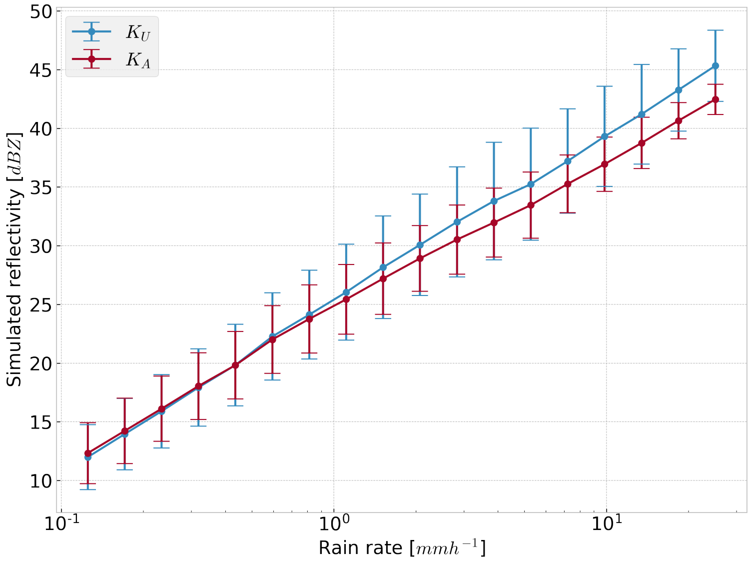

Figure 9. Simulated radar reflectivities at the two DPR frequencies, K_U and K_A bands, shown as means and standard deviations ($\pm 1\sigma$) binned by rain rate. The rain rate and the DSD are directly from OceanRAIN observations.

Rayleigh regime or partly in the Mie regime. The K_A band is less effected by DSD variations in both the passive and active simulations while scaling mostly linearly with increasing RWC or rain rate.

6 Summary and conclusions

This study has investigated the variability of raindrop size distributions over the global oceans in a variety of contexts relevant to retrievals and atmospheric modeling. Methods to attach a functional form to raindrop populations vary, but have largely been predicated on limited land-based observations in the past. The OceanRAIN observation network of disdrometers provides an opportunity to move towards better understanding of global raindrop populations, with ramifications in aid of satellite retrievals and model parameterizations, which are necessarily global in scope.

The disdrometer data were shown to have limited dependence on latitude or SST (Fig. 1) when quantified using parameters of the normalized gamma distribution (Eq. 3). The mean and median of D_m tend to vary within $0.1\,\mathrm{mm}$ across all regions, with $\pm\sigma$ of about $0.2\,\mathrm{mm}$. Most observations of $log_{10}(N_w)$ fall within 3.0 to 4.3, with a weak correlation observed between N_w and SST. These parameters from OceanRAIN were also compared to the leading estimates from a satellite platform (Fig. 2); comparisons with GPM matched relatively well for distributions of D_m but less so for N_w. Both parameters appear to be too peaked from the GPM retrieval, likely a result of strong influence from that retrieval's a priori state as $D_m = 1.0$ and $log_{10}(N_w) = 4.0$ was commonly seen. The data sets observe similar spreads in the distributions of D_m, but the disdrometers observe significantly more variability in N_w than seen by GPM; the middle 90% of GPM N_w retrievals fall within one order of magnitude, whereas the middle 90% of disdrometer observations span 2.2 orders of magnitude. It is speculated that the GPM retrievals may be over-constrained, although it was expected that the point measurements of the disdrometer would display greater variability than those from satellite sources due to spatial considerations alone.

Usage of the normalized gamma function to encapsulate the observed DSD behavior was questioned, as it appears more applicable in the Tropics than for higher latitude populations (Fig. 4). Its use can cause systematic biases in rain rate estimation, quantified to be in the mean a -2% error relative to total accumulation calculated with the raw disdrometer size data. This is a relatively small error for total accumulation because the smallest drops that are most misrepresented by the normalized gamma formalism account for relatively little of the total mass flux, however for about 3% of cases this is an error of $-0.5\,\mathrm{mm\,h^{-1}}$ or more, and can thus be significant. For many applications, an exponential DSD would be simpler and more appropriate than a MGD for oceanic rainfall (Fig. 3), but of course does not encapsulate the range of variability that exists, which may be better represented by a generalized gamma approach (Thurai and Bringi, 2018).

Radiative properties of raindrop populations can vary rapidly for low frequency microwaves, manifest in Fig. 8 as uncertainty makes up approximately half the radiative signal at 18 GHz but much less at higher frequencies. This is because the presence of a few larger drops can cause non-negligible Mie scattering that impacts the otherwise emission-dominated radiative signal and Rayleigh scattering from smaller drops, an effect that diminishes as frequency increases. Fig. 9 also showed this effect, with lower frequencies exhibiting greater uncertainty for a given RWC or rain rate due to observed DSD variability. Whereas the radiative uncertainty is similar for light rain rates, modeled variability can be 2-3 times greater at K_U rather than K_A band, true for passive and active simulations. These ranges of forward model variability however represent a worst case scenario for satellite retrievals or data assimilation, as any skill in assuming or retrieving the DSD would shrink these ranges. This passive forward model variability can even be viewed favorably, as it demonstrates sensitivity to the DSD at low frequencies that may aid DSD retrievals. Simulations comparing forward model errors caused by using a GMM-derived or MGD state compared to the true DSD state showed that a high N_{GMM} value was needed for the GMM states to outperform the 3-moment MGD for forward model errors (not shown). This is in line with Fig. 7, but also indicative that it is hard for a single-moment scheme such as GMM to compete without having a large number of possible states.

This exploration of DSD shape “distinctiveness” was motivated by the remote sensing and modeling communities’ need for simple but accurate parameterizations of rainwater’s size distribution. For instance, if a region or rainfall regime tends to exhibit one or two DSD shapes, this simplifies a multidimensional problem considerably. The results, however, demonstrate that simple separation of DSD shapes by latitude and SST, or by other variables such as dewpoint temperature and RWC (not shown), does not significantly simplify the DSD problem. The limited spatiotemporal sampling of OceanRAIN meant that further subdivision of regional data for seasonal shifts in DSD was not possible. The conclusion is then that global oceanic DSD variability, though more uniform than over land surfaces, is complex and not easily reduced to a single moment parameterization or a small set of possible shapes.

Code availability. The code used for analysis is all available in the form of iPython notebooks via a Zenodo archive, found in the references.

Author contributions. DD and PE conceived and designed the study, inspired by discussions with and the work of CK and DJ. DD performed the analysis with aid from SP. DD wrote the manuscript and all authors contributed to its final form.

Competing interests. The authors declare that they have no conflict of interest.

Acknowledgements. This study was funded with support from the Swedish National Space Agency.

References

Atlas, D. and Ulbrich, C. W.: Path- and Area-Integrated Rainfall Measurement by Microwave Attenuation in the 1–3 cm Band, J. Appl. Meteorol., 16, 1322–1331, https://doi.org/10.1175/1520-0450(1977)016<1322:PAAIRM>2.0.CO;2, 1977.

Berg, W., L'Ecuyer, T., and Kummerow, C.: Rainfall climate regimes: The relationship of regional TRMM rainfall biases to the environment, J. Appl. Meteorol. and Climatol., 45, 434–454, https://doi.org/10.1175/JAM2331.1, 2006.

Bringi, V. N., Chandrasekar, V., Hubbert, J., Gorgucci, E., Randeu, W. L., and Schoenhuber, M.: Raindrop size distribution in different climatic regimes from disdrometer and dual-polarized radar analysis, J. Atmos. Sci., 60, 354–365, https://doi.org/10.1175/1520-0469(2003)060<0354:RSDIDC>2.0.CO;2, 2003.

Buehler, S. A., Mendrok, J., Eriksson, P., Perrin, A., Larsson, R., and Lemke, O.: ARTS, the Atmospheric Radiative Transfer Simulator – version 2.2, the planetary toolbox edition, Geosci. Model Dev., 11, 1537–1556, https://doi.org/10.5194/gmd-11-1537-2018, 2018.

Bumke, K. and Seltmann, J.: Analysis of measured drop size spectra over land and sea, ISRN Meteorol., 2012, https://doi.org/10.5402/2012/296575, 2011.

Burdanowitz, J., Klepp, C., Bakan, S., and Buehler, S. A.: Towards an along-track validation of HOAPS precipitation using OceanRAIN optical disdrometer data over the Atlantic Ocean, Quart. J. Roy. Meteor. Soc., 144, 235–254, https://doi.org/10.1002/qj.3248, https://rmets.onlinelibrary.wiley.com/doi/abs/10.1002/qj.3248, 2018.

Dolan, B., Fuchs, B., Rutledge, S. A., Barnes, E. A., and Thompson, E. J.: Primary Modes of Global Drop Size Distributions, J. Atmos. Sci., 75, 1453–1476, https://doi.org/10.1175/JAS-D-17-0242.1, 2018.

Duncan, D. I.: Supporting code for ACP submission on DSD distinctiveness, https://doi.org/10.5281/zenodo.2539161, 2019.

Duncan, D. I., Kummerow, C. D., Dolan, B., and Petković, V.: Towards variational retrieval of warm rain from passive microwave observations, Atmos. Meas. Tech., 11, 4389–4411, https://doi.org/10.5194/amt-11-4389-2018, https://www.atmos-meas-tech.net/11/4389/2018/, 2018.

Eriksson, P., Buehler, S., Davis, C., Emde, C., and Lemke, O.: ARTS, the Atmospheric Radiative Transfer Simulator, version 2, J. Quant. Spectrosc. Radiat. Transfer, 112, 1551–1558, https://doi.org/10.1016/j.jqsrt.2011.03.001, 2011.

Grecu, M., Olson, W. S., Munchak, S. J., Ringerud, S., Liao, L., Haddad, Z., Kelley, B. L., and McLaughlin, S. F.: The GPM Combined Algorithm, J. Atmos. Oceanic Technol., 33, 2225–2245, https://doi.org/10.1175/JTECH-D-16-0019.1, 2016.

Grossklaus, M., Uhlig, K., and Hasse, L.: An optical disdrometer for use in high wind speeds, J. Atmos. Oceanic Technol., 15, 1051–1059, https://doi.org/10.1175/1520-0426(1998)015<1051:AODFUI>2.0.CO;2, 1998.

Hou, A. Y., Kakar, R. K., Neeck, S., Azarbarzin, A. A., Kummerow, C. D., Kojima, M., Oki, R., Nakamura, K., and Iguchi, T.: The Global Precipitation Measurement Mission, Bull. Amer. Meteor. Soc., 95, 701–722, https://doi.org/10.1175/BAMS-D-13-00164.1, 2014.

Illingworth, A. J. and Blackman, T. M.: The Need to Represent Raindrop Size Spectra as Normalized Gamma Distributions for the Interpretation of Polarization Radar Observations, J. Appl. Meteorol., 41, 286–297, https://doi.org/10.1175/1520-0450(2002)041<0286:TNTRRS>2.0.CO;2, 2002.

Jones, D. C., Holt, H. J., Meijers, A. J. S., and Shuckburgh, E.: Unsupervised clustering of Southern Ocean Argo float temperature profiles, J. Geophys. Res. Oceans, 0, https://doi.org/10.1029/2018JC014629, 2019.

Klepp, C.: The oceanic shipboard precipitation measurement network for surface validation — OceanRAIN, Atmos. Res., 163, 74 – 90, https://doi.org/https://doi.org/10.1016/j.atmosres.2014.12.014, http://www.sciencedirect.com/science/article/pii/S0169809515000034, 6th Workshop of the International Precipitation Working Group, 2015.

Klepp, C., Michel, S., Protat, A., Burdanowitz, J., Albern, N., Louf, V., Bakan, S., Dahl, A., and Thiele, T.: Ocean Rainfall And Ice-phase precipitation measurement Network - OceanRAIN-M, https://doi.org/10.1594/WDCC/OceanRAIN-M, 2017.

Klepp, C., Michel, S., Protat, A., Burdanowitz, J., Albern, N., Kähnert, M., Dahl, A., Louf, V., Bakan, S., and Buehler, S. A.: OceanRAIN, a new in-situ shipboard global ocean surface-reference dataset of all water cycle components, Sci. Data, 5, 180 122, https://doi.org/10.1038/sdata.2018.122, 2018.

Kummerow, C. D., Randel, D. L., Kulie, M., Wang, N.-Y., Ferraro, R., Joseph Munchak, S., and Petkovic, V.: The evolution of the Goddard profiling algorithm to a fully parametric scheme, J. Atmos. Oceanic Technol., 32, 2265–2280, https://doi.org/10.1175/JTECH-D-15-0039.1, 2015.

Lebsock, M. D., Stephens, G. L., and Kummerow, C.: Multisensor satellite observations of aerosol effects on warm clouds, J. Geophys. Res. Atmos., 113, https://doi.org/10.1029/2008JD009876, 2008.

Leinonen, J., Moisseev, D., Leskinen, M., and Petersen, W. A.: A Climatology of Disdrometer Measurements of Rainfall in Finland over Five Years with Implications for Global Radar Observations, J. Appl. Meteorol. Climatol., 51, 392–404, https://doi.org/10.1175/JAMC-D-11-056.1, 2012.

Loew, A., Bell, W., Brocca, L., Bulgin, C. E., Burdanowitz, J., Calbet, X., Donner, R. V., Ghent, D., Gruber, A., Kaminski, T., Kinzel, J., Klepp, C., Lambert, J.-C., Schaepman-Strub, G., Schröder, M., and Verhoelst, T.: Validation practices for satellite-based Earth observation data across communities, Rev. Geophys., 55, 779–817, https://doi.org/10.1002/2017RG000562, https://agupubs.onlinelibrary.wiley.com/doi/abs/10.1002/2017RG000562, 2017.

Marshall, J. S. and Palmer, W. M. K.: The distribution of raindrops with size, J. Meteor., 5, 165–166, https://doi.org/10.1175/1520-0469(1948)005<0165:TDORWS>2.0.CO;2, 1948.

Mason, S. L., Chiu, J. C., Hogan, R. J., and Tian, L.: Improved rain rate and drop size retrievals from airborne Doppler radar, Atmos. Chem. Phys., 17, 11 567—11 589, https://doi.org/10.5194/acp-17-11567-2017, 2017.

Maze, G., Mercier, H., Fablet, R., Tandeo, P., Radcenco, M. L., Lenca, P., Feucher, C., and Goff, C. L.: Coherent heat patterns revealed by unsupervised classification of Argo temperature profiles in the North Atlantic Ocean, Prog. Oceanogr., 151, 275–292, https://doi.org/https://doi.org/10.1016/j.pocean.2016.12.008, http://www.sciencedirect.com/science/article/pii/S0079661116300714, 2017.

Munchak, S. J., Kummerow, C. D., and Elsaesser, G.: Relationships between the raindrop size distribution and properties of the environment and clouds inferred from TRMM, J. Climate, 25, 2963–2978, https://doi.org/10.1175/JCLI-D-11-00274.1, 2012.

Olson, W.: GPM DPR and GMI (Combined Precipitation) L3 1 month 0.25 degree x 0.25 degree V06, https://doi.org/10.5067/GPM/DPRGMI/CMB/3B-MONTH/05, 2017.

Pedregosa, F., Varoquaux, G., Gramfort, A., Michel, V., Thirion, B., Grisel, O., Blondel, M., Prettenhofer, P., Weiss, R., Dubourg, V., Vanderplas, J., Passos, A., Cournapeau, D., Brucher, M., Perrot, M., and Duchesnay, E.: Scikit-learn: Machine Learning in Python, J. Mach. Learn. Res., 12, 2825–2830, 2011.

Petković, V., Kummerow, C. D., Randel, D. L., Pierce, J. R., and Kodros, J. K.: Improving the Quality of Heavy Precipitation Estimates from Satellite Passive Microwave Rainfall Retrievals, J. Hydrometeorol., 19, 69–85, https://doi.org/10.1175/JHM-D-17-0069.1, 2018.

Petty, G. W. and Huang, W.: The Modified Gamma Size Distribution Applied to Inhomogeneous and Nonspherical Particles: Key Relationships and Conversions, J. Atmos. Sci., 68, 1460–1473, https://doi.org/10.1175/2011JAS3645.1, 2011.

Prigent, C., Aires, F., Wang, D., Fox, S., and Harlow, C.: Sea-surface emissivity parametrization from microwaves to millimetre waves, Quart. J. Roy. Meteor. Soc., 143, 596–605, https://doi.org/10.1002/qj.2953, 2017.

Smith, P. L.: Raindrop Size Distributions: Exponential or Gamma—Does the Difference Matter?, J. Appl. Meteorol., 42, 1031–1034, https://doi.org/10.1175/1520-0450(2003)042<1031:RSDEOG>2.0.CO;2, 2003.

Tapiador, F. J., Haddad, Z. S., and Turk, J.: A Probabilistic View on Raindrop Size Distribution Modeling: A Physical Interpretation of Rain Microphysics, J. Hydrometeorol., 15, 427–443, https://doi.org/10.1175/JHM-D-13-033.1, 2014.

Testud, J., Oury, S., Black, R. A., Amayenc, P., and Dou, X.: The concept of "normalized" distribution to describe raindrop spectra: A tool for cloud physics and cloud Remote Sens., J. Appl. Meteorol., 40, 1118–1140, https://doi.org/10.1175/1520-0450(2001)040<1118:TCONDT>2.0.CO;2, 2001.

Thompson, E. J., Rutledge, S. A., Dolan, B., and Thurai, M.: Drop Size Distributions and Radar Observations of Convective and Stratiform Rain over the Equatorial Indian and West Pacific Oceans, J. Atmos. Sci., 72, 4091–4125, https://doi.org/10.1175/JAS-D-14-0206.1, 2015.

Thompson, E. J., Rutledge, S. A., Dolan, B., Thurai, M., and Chandrasekar, V.: Dual-Polarization Radar Rainfall Estimation over Tropical Oceans, J. Appl. Meteorol. Climatol., 57, 755–775, https://doi.org/10.1175/JAMC-D-17-0160.1, 2018.

Thurai, M. and Bringi, V. N.: Application of the Generalized Gamma Model to Represent the Full Rain Drop Size Distribution Spectra, J. Appl. Meteorol. Climatol., 57, 1197–1210, https://doi.org/10.1175/jamc-d-17-0235.1, 2018.

Thurai, M., Bringi, V. N., and May, P. T.: CPOL Radar-Derived Drop Size Distribution Statistics of Stratiform and Convective Rain for Two Regimes in Darwin, Australia, J. Atmos. Oceanic Technol., 27, 932–942, https://doi.org/10.1175/2010JTECHA1349.1, 2010.

Thurai, M., Gatlin, P., Bringi, V., Petersen, W., Kennedy, P., Notaroš, B., and Carey, L.: Toward completing the raindrop size spectrum: Case studies involving 2D-video disdrometer, droplet spectrometer, and polarimetric radar measurements, J. Appl. Meteorol. Climatol., 56, 877–896, https://doi.org/10.1175/JAMC-D-16-0304.1, 2017.

Ulbrich, C. W.: Natural variations in the analytical form of the raindrop size distribution, J. Climate Appl. Meteor., 22, 1764–1775, https://doi.org/10.1175/1520-0450(1983)022<1764:NVITAF>2.0.CO;2, 1983.

Williams, C. R.: Reflectivity and Liquid Water Content Vertical Decomposition Diagrams to Diagnose Vertical Evolution of Raindrop Size Distributions, J. Atmos. Oceanic Technol., 33, 579–595, https://doi.org/10.1175/JTECH-D-15-0208.1, 2016.

Williams, C. R. and Gage, K. S.: Raindrop size distribution variability estimated using ensemble statistics, Ann. Geophys., 27, 555–567, https://doi.org/10.5194/angeo-27-555-2009, https://www.ann-geophys.net/27/555/2009/, 2009.

Williams, C. R., Bringi, V. N., Carey, L. D., Chandrasekar, V., Gatlin, P. N., Haddad, Z. S., Meneghini, R., Munchak, S. J., Nesbitt, S. W., Petersen, W. A., Tanelli, S., Tokay, A., Wilson, A., and Wolff, D. B.: Describing the Shape of Raindrop Size Distributions Using Uncorrelated Raindrop Mass Spectrum Parameters, J. Appl. Meteorol. Climatol., 53, 1282–1296, https://doi.org/10.1175/JAMC-D-13-076.1, 2014.